Journal of Alloys and Compounds 637 (2015) 407–417

Contents lists available at ScienceDirect

Journal of Alloys and Compounds

journal homepage: www.elsevier.com/locate/jalcom

# Dynamics of the incorporation of Co into the wurtzite ZnO matrix and its magnetic properties

A. Mesquita [a,1], F.P. Rhodes [b], R.T. da Silva [a], P.P. Neves [a], A.O. de Zevallos [a], M.R.B. Andreeta [c], M.M. de Lima Jr. [d], A. Cantarero [d], I.S. da Silva [e], M.A. Boselli [e], X. Gratens [f], V.A. Chitta [f], A.C. Doriguetto [a], W.B. Ferraz [g], A.C.S. Sabioni [b], H.B. de Carvalho [a,*]

[a] Universidade Federal de Alfenas, Alfenas, MG, Brazil
[b] Universidade Federal de Ouro Preto, Ouro Preto, MG, Brazil
[c] Departamento de Engenharia de Materiais, Universidade Federal de São Carlos, São Carlos, SP, Brazil
[d] University of Valencia, Materials Science Institute, Valencia, Spain
[e] Universidade Federal de Uberlândia, Uberlândia, MG, Brazil
[f] Instituto de Física da Universidade de São Paulo, São Paulo, SP, Brazil
[g] Centro de Desenvolvimento de Tecnologia Nuclear/CNEN, Belo Horizonte, MG, Brazil

ARTICLE INFO

*Article history:*
Received 17 December 2014
Received in revised form 5 February 2015
Accepted 1 March 2015
Available online 5 March 2015

*Keywords:*
Spintronic
Dilute magnetic oxide
$Zn_{1-x}Co_xO$
Phase diagram
Magnetic properties
Co distribution

ABSTRACT

Bulk Co-doped ZnO ($Zn_{1-x}Co_xO$) samples were prepared and studied with particular emphasis on their compositions, structures, and magnetic properties. A detailed microstructural analysis was conducted to investigate the nature of Co incorporation into the wurtzite ZnO matrix. The $Zn_{1-x}Co_xO$ ceramic samples were prepared using the standard solid-state reaction method with different Co molar concentrations of up to 30%. A Co solubility limit of approximately 23% was determined. For samples with Co concentrations greater than 23%, a segregated phase identified as Zn-doped CoO ($Co_{1-y}Zn_yO$ with $y = 0.23$) was observed. The magnetic characterization for the single-phase samples revealed a paramagnetic behavior with antiferromagnetic coupling of $Co^{2+}$ ions within the ZnO matrix. In order to get more insight about the magnetic results Monte Carlo simulations were conducted for different magnetic couplings and different Co distributions over the volume of the samples. We discussed the observed magnetic behavior of our samples by considering the main theories regarding the magnetic properties of dilute magnetic oxides. An inhomogeneous distribution of Co ions within the grains was inferred from the microstructural and magnetic characterization.

## 1. Introduction

Ferromagnetism (FM) in the transition metal (TM) doped ZnO system has attracted much interest in the last decade due to its potential application in spintronic devices [1–3]. Spin injection in semiconductors is a fundamental problem in the development of commercial spintronic devices due to the well-known impedance mismatch between semiconductors and ferromagnetic materials [4]. To overcome this issue, III–V diluted magnetic semiconductors (DMS) have emerged as a powerful solution [5,6] that can introduce new functionalities that are difficult to implement in metallic structures, such as the electrical control of the coercivity [7] and the Curie temperature ($T_C$) [8]. However it was impossible to observe ferromagnetism at room temperature in these compounds, which inhibited their application in devices.

Studies in the ZnO matrix have been motivated by the calculations of Dietl et al., which predict room temperature ferromagnetism (RTFM) for Mn-doped GaN and ZnO [9]. Following this theoretical work, many experimental studies were conducted using a ZnO matrix doped with different TM [10]. Although many experimental studies have reported $T_C$ values above room temperature [1], many groups have shown different results: ferromagnetism with different Curie temperatures [2,3], paramagnetism [11], and even spin glass behavior [12]. Some reports have attributed the observed RTFM to the formation of a magnetic secondary phase [13] and TM-rich nanocrystals [14]. Furthermore, surprising experimental reports have presented RTFM in undoped systems [15]. Different results have been reported for similar systems, which indicated that magnetization in TM-doped ZnO

---

* Corresponding author.
*E-mail address:* bonette@unifal-mg.edu.br (H.B. de Carvalho).

[1] Present address: Departamento de Física, Instituto de Geociências e Ciências Exatas, Universidade Estadual Paulista, Rio Claro, SP, Brazil.

http://dx.doi.org/10.1016/j.jallcom.2015.03.004
0925-8388/

($Zn_{1-x}TM_xO$) strongly depends on the preparation parameters and the processes conditions [16]. In addition to the trivial extrinsic origins of the RTFM that result from the ferromagnetic secondary phases, the main theoretical models that are currently available for describing the origins and properties of the observed RTFM are all linked to structural defects. This linkage explains why the ferromagnetic properties are rarely reproducible. For TM-doped systems, the theoretical models assume that the electrons, introduced by donor defects into the conduction band [17] or forming bound magnetic polarons (BMPs) [18], mediate the ferromagnetic couplings between the TM ions. Moreover, the ferromagnetic response of the undoped systems is assigned to the spins of the electrons that reside at the points or extended defects, the so called $d^0$ ferromagnetism [19]. Before elucidating the mechanisms of intrinsic FM, the measured magnetic hysteresis loops must be classified as intrinsic or extrinsic. Contamination by magnetic elements [20], measurement errors [21] and segregated secondary phases [13,22] can all cause ferromagnetic signals. Therefore, the study and determination of the phase diagram of ZnO and TM oxides is important to assure the synthesis of TM-doped ZnO ($Zn_{1-x}TM_xO$) diluted magnetic semiconductors. Among the TM elements used to dope ZnO, Co deserves special attention since it has one of the highest magnetic moments (4.8 $\mu_B$) and a positive magnetic exchange coupling constant in the metallic phase. Specifically, for the $Zn_{1-x}Co_xO$ system, only a few reports are available that consider the equilibrium diagram of Zn–Co–O compounds in a system. Relatively higher Co solubility limit values can be reached for ZnO by using non-equilibrium synthesis [23], low temperatures [24], and by decreasing the grain size [25]. The study conducted by Straumal et al. [26] deserves special consideration. These authors showed that by decreasing the grain size of polycrystalline systems, the Co solubility limit increased. This behavior was attributed to the formation of TM-enriched layers at the grain boundaries, which shifted the solubility limits of these elements in ZnO toward higher concentrations. Concerning bulk systems, complete phase equilibrium-temperature diagram was only recently published by Perry and Mason [27]. In that study, the authors demonstrated the increasing solubility of Co in ZnO with increasing temperature. Beyond the solubility limit and at high temperatures, a Zn-doped CoO ($Co_{1-y}Zn_yO$) phase precipitated.

In this work, we report the mechanisms of Co incorporation and the segregation processes of Co rich phases, determining the Co solubility limit, in $Zn_{1-x}Co_xO$ bulk samples with nominal Co molar concentrations of up to 30 at.% that were prepared using the standard solid-state reaction method at 1400 °C. We performed a detailed microstructural analyses by conjugating several different techniques to fully characterize the samples structures. The relationships between the magnetic properties and the structure results of the $Zn_{1-x}Co_xO$ bulk samples are presented and analyzed under the scope of the current theoretical models.

## 2. Experimental section

Polycrystalline $Zn_{1-x}Co_xO$ bulk samples with nominal concentrations ($x_N = 0.15$, 0.20, 0.25, 0.30, 0.35 and 0.50) were prepared by using the standard solid-state reaction method. The last two samples were prepared in a second round to increase the statistical analysis and were not available for measurements by all techniques. The stoichiometric amounts of ZnO (99.998%) and $Co_3O_4$ (99.7%) were mixed and ball milled for 5 h using Zn spheres. The resulting powder was cold compacted at a pressure of 600 MPa in the form of pellets (green pellets). These pellets were finally sintered under an oxygen atmosphere at 1400° C for 4 h.

Scanning electron microscope (SEM) images of the samples were acquired using a SEM-LV JEOL JSM 5900 backscattered electron detector (BSE) with a resolution of 3 nm at 30 kV. High-resolution transmission electron microscopy (HRTEM) and Selected Area Electron Diffraction (SAED) studies were performed on cross-sectional samples that were prepared by standard mechanical polishing followed by $Ar^+$-ion milling (Fishione 1010) by using a TECNAI G2 F20 Field Emission Gun (FEG) microscope that was operated at 200 kV. The structures of the $Zn_{1-x}Co_xO$ bulk samples were investigated using powder X-ray diffraction (XRD) measurements with a Rigaku Ultima IV employing Cu K$\alpha$ radiation ($\lambda = 1.5418$ Å). Structural analysis was performed using the Rietveld method and was implemented using the software package GSAS [28,29]. Raman spectroscopy was carried out at room temperature using a confocal microscope (WiTec Alpha 300 S – A/R) and an $Ar^+$ laser for excitation (514.5 nm/15 mW). All images were acquired for an area of $50 \times 50$ $(\mu m)^2$ with a resolution of $100 \times 100$ points per image and an integration time of 60 ms per point. The WiTec Project 2.06 program was used for data processing. Since our samples are polycrystalline, we do not track the light polarization in the Raman experiments. Next, X-ray absorption spectroscopy (XAS) measurements were performed in transmittance mode at the XAS beamline at the Brazilian Synchrotron Light Laboratory (LNLS), Campinas, Brazil. The EXAFS (Extended X-ray Absorption Fine Structure) spectra were extracted using the Multi-Platform Applications for X-ray absorption (MAX) software package, [30] and theoretical spectra were calculated using the FEFF9 code [31]. The magnetic measurements were performed using a Superconducting Quantum Interference Device magnetometer (SQUID).

## 3. Results and discussion

### 3.1. Electron microscopy and elemental analyses

Fig. 1 shows SEM images that were acquired over the polished surface of the $Zn_{1-x}Co_xO$ samples. A series of full scans over large areas confirms the absence of microclusters in the samples with $x_N = 0.15$ and 0.20 (Fig. 2(a) and (b)), while a segregated phase can be identified in the SEM images for the samples with $x_N = 0.25$ and 0.30 (grains indicated by purple[2] color in Fig. 1(c) and (d)). We did not observe significant differences in the bulk density (porosity) among the whole set of the studied samples. The average density of the samples, measured by the water displacement (Archimedes) method, is of around 93%.

Energy dispersive spectroscopy (EDS) measurements were performed to accurately determine the elemental compositions of the two identified phases. Representative EDS spectra corresponding to the analyses performed in the areas indicated by the crosses in Fig. 1(a)–(d) are shown in Fig. 1(e). In the ZnO matrix, both Zn and Co are detected, indicating that the active incorporation of Co into the ZnO matrix was achieved for all of the samples, including the samples where segregation appears. The solubility limits of the Co in our $Zn_{1-x}Co_xO$ bulk samples were evaluated by plotting the effective Co concentrations ($x_E$) of the ZnO matrix as a function of the nominal Co concentration ($x_N$), Fig. 1(f). We observed that the measured and nominal concentration values were similar for $x_N = 0.15$ and 0.20. For samples with $x_N \geqslant 0.25$, segregation occurs after the solubility limit is achieved, and an abrupt deviation of $x_E$ in respect to the $x_N$ occurs. The maximum Co concentration achieved in the ZnO matrix, the Co solubility limit, is $22.8 \pm 0.1$ at.%. This value agrees with the solubility limit that is obtained by extrapolation from the diagram presented by Perry and Mason [27] and the diagram of the polycrystalline samples presented by Straumal et al. [26] with grain sizes of more than 1 μm. For samples with $x_N$ values that are beyond the solubility limit, the EDS data reveals that the segregated phase corresponds to Co-rich clusters, where Co and Zn elements are both present. In addition, this result agrees with the phase diagram presented by Perry et al., where the segregated phase is a Zn-doped rocksalt CoO ($Co_{1-y}Zn_yO$) compound. To emphasize the structural distinction between the Co-rich and Zn-rich samples, we use $Co_{1-y}Zn_yO$ for the first compound and $Zn_{1-x}Co_xO$ for the second compound. As shown in Fig. 1(f), the values for $y$ are nearly the same as those of the Co solubility limit, with an average value that is slightly greater (i.e., $23.4 \pm 0.1$ at.%). The similarities between the observed cross-doping concentration ($x \cong y \cong 0.23$) of the $Zn_{1-x}Co_xO$ and $Co_{1-y}Zn_yO$ phases indicate equilibrium conditions between the

---

[2] For interpretation of color in Fig. 1, the reader is referred to the web version of this article.

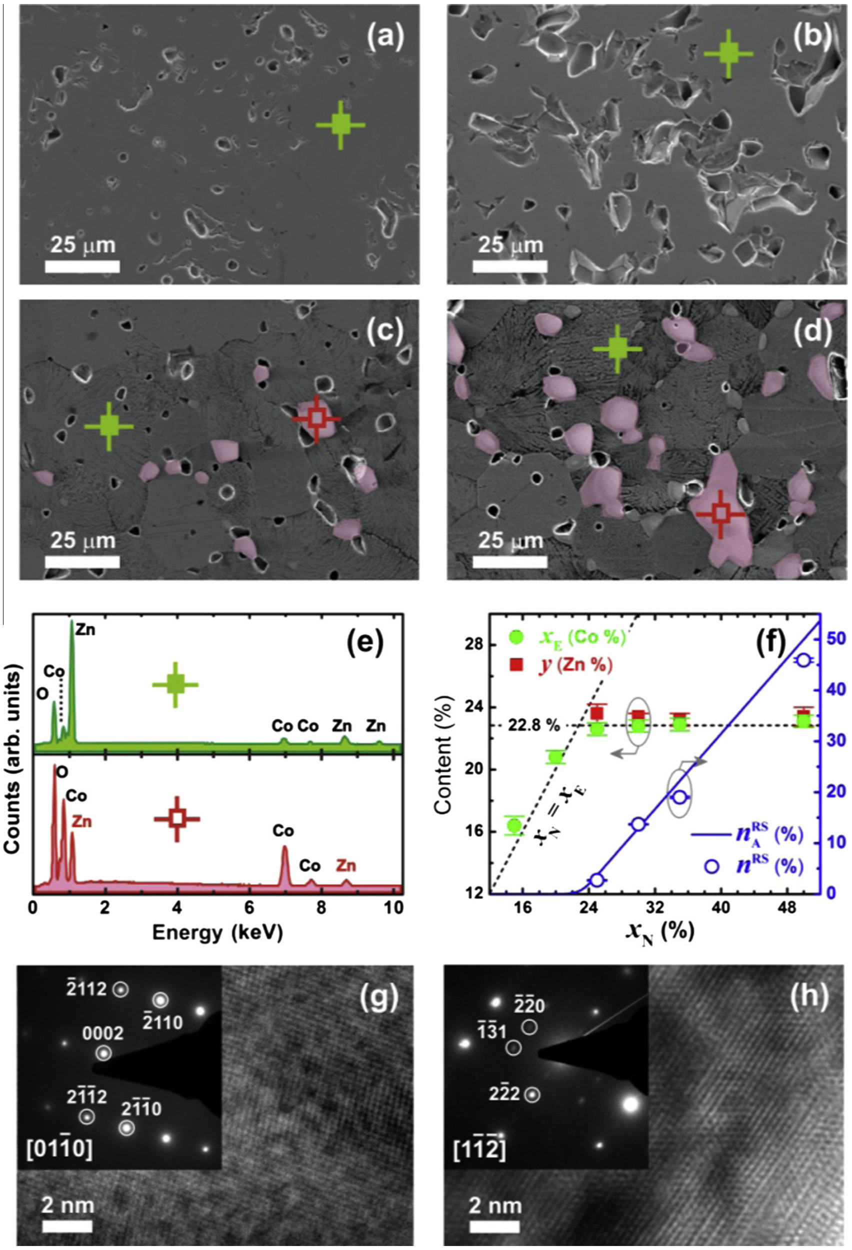

**Fig. 1.** SEM images for the $Zn_{1-x}Co_xO$ samples with (a) $x_N = 0.15$, (b) $x_N = 0.20$, (c) $x_N = 0.25$ and (d) $x_N = 0.30$. The secondary phase is identified in (c) and (d). (e) EDS spectra acquired for the Co-doped ZnO matrix (full cross) and the segregated CoO phase (open cross) of the samples. (f) Elemental concentrations ($x_E$ and $y$) obtained using EDS measurements and the molar fraction of the segregated CoO phase ($n_A^{RS}$, analytically calculated, and $n^{RS}$, determined by Rietveld refinement) as a function of the nominal Co concentration ($x_N$). All of the data are presented in percentages. The HRTEM micrographs of the (g) $Zn_{0.77}Co_{0.23}O$ and (h) $Co_{0.77}Zn_{0.23}O$ grains of the sample with $x_N = 0.30$. The insets present the SAED patterns of the enclosed areas.

cation diffusion under the synthesis conditions. This behavior is expected because Zn and Co have very similar physical and chemical characteristics.

The HRTEM analysis was conducted for the $Zn_{0.77}Co_{0.23}O$ (Fig. 1(g)) and $Co_{0.77}Zn_{0.23}O$ (Fig. 1(h)) grains of the sample with $x_N = 0.30$ to investigate the structures of the phases. At this scale, no visual evidence of cross-contamination was found, indicating the single-crystal nature of each grain. This single-crystal nature was confirmed by the SAED patterns (insets of Fig. 1(g) and (h)). For $Zn_{0.77}Co_{0.23}O$, the SAED analyses (Fig. 1(g)) indicated a single hexagonal wurtzite ZnO structure (zone axis $[01\bar{1}0]$). For the $Co_{0.77}Zn_{0.23}O$ grain (Fig. 1(h)), the acquired diffraction pattern corresponded to the rocksalt CoO structure (zone axis $[1\bar{1}\bar{2}]$). In both cases, no satellite diffraction spot, apart from that of the main cited structures, was detected.

### 3.2. X-ray diffraction

Fig. 2(a) shows the XRD results for the $Zn_{1-x}Co_xO$ samples as a function of the Co content. The observed peaks correspond to those expected for polycrystalline hexagonal wurtzite (W) ZnO, space group $P6_3mc$ [32]. The relatively narrow line-widths revealed a highly crystalline quality for all of the samples. No indication of additional phases was observed within the detection limit of the measurements for the samples with $x_N = 0.15$ and 0.20. A segregated phase was identified for the samples with $x_N = 0.25$ and 0.30.

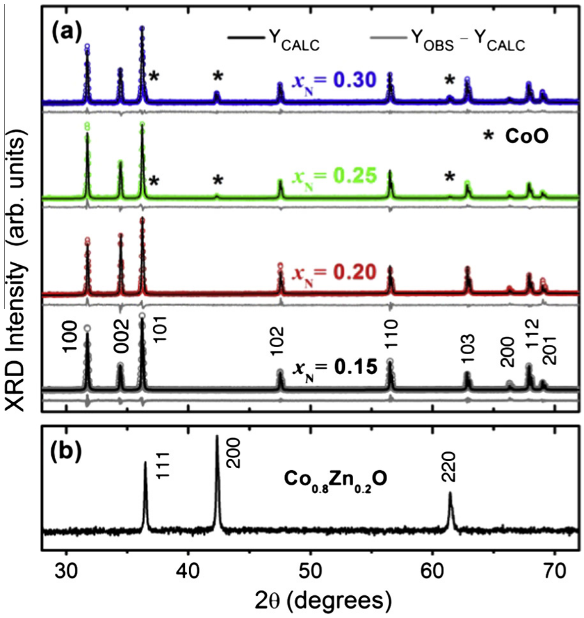

**Fig. 2.** (a) Refined XRD pattern of the polycrystalline $Zn_{1-x}Co_xO$ bulk samples for different Co contents. The experimental and calculated profiles are represented by open symbols (circles) and solid curves, respectively. The lower curve in each panel is the difference plot. The asterisks show the peak positions of the segregated CoO phase [33]. The corresponding refinement results are presented in Table 1. (b) The XRD diffraction pattern of a Zn-doped CoO ($Co_{0.8}Zn_{0.2}O$) bulk sample.

The diffraction peaks associated with the segregated phase are indicated with asterisks in Fig. 2(a) and are related to the rocksalt (R) CoO phase with a Fm-*3m* space group [33], confirming previous analyses. These results indicate that the solubility limit of Co in the ZnO matrix is between 20 and 25 at.% of the nominal Co content for the studied samples.

The Rietveld refinements of the XRD data were initiated with $Zn^{2+}$ and $O^{2-}$ atoms located at (1/3, 2/3, 0) and (1/3, 2/3, $z$), respectively. The results obtained from the Rietveld refinement are shown in Fig. 2(a) and Table 1, and indicate good agreement between the experimental and calculated patterns. No significant changes were observed in the wurtzite cell lattice parameters as the Co concentration increased. In addition, these values were similar to those found in the literature for pure ZnO [32]. The Rietveld results were expected considering that the $Co^{2+}$ ions (tetrahedral ionic radius = 0.58 Å) replace the $Zn^{2+}$ ions (tetrahedral ionic radius = 0.60 Å) in the ZnO wurtzite matrix. The XRD results indicate that the Co in our $Zn_{1-x}Co_xO$ bulk samples have a 2+ oxidation state and are located at the sites of the $Zn^{2+}$ cations. The 2+ oxidation state of the Co was further confirmed from the local structure analysis.

The atom occupation factors were also determined by using a Rietveld refinement for all samples. These data are presented in Table 2. By using the atom occupation factor, it is possible to infer the density of the defects that are related to the Zn and O vacancies. As shown in Table 2, within the experimental error, the occupancy coincides with the nominal content. Thus, no expressive number of vacancies occurs on the anion and on the cation sites of the $Zn_{1-x}Co_xO$ bulk samples. In addition, the Co solubility limit can be extracted from the atom occupation factor. For samples with $x_N > 0.20$, the Co occupation factor is nearly constant and equals 22.6 ± 0.2 at.% (average value). Therefore, the Co solubility limit in our samples is approximately 23 at.%, which corresponds with the EDS results. Likewise, the Zn contents in the rocksalt $Co_{1-y}Zn_yO$ segregated phase ($y$) are constant and equal to approximately 23.2 ± 0.3 at.% (average value). These data agree with the results obtained by the EDS measurements.

**Table 1**
Structural data for the samples obtained through the Rietveld refinement. Here, $\chi^2$ is the square of goodness-of-fit indicator and $R_{WP}$ is the refinement quality parameter. In addition, $n^{RS}$ is the percentage of the $Co_{0.77}Zn_{0.23}O$ segregated phase.

| $x_N$ | $a$ (Å) | $c$ (Å) | $R_{WP}$ | $\chi^2$ | $n^{RS}$ (%) |
|---|---|---|---|---|---|
| 0.15 | 3.2527(1) | 5.2048(1) | 15.37 | 5.31 | – |
| 0.20 | 3.2535(2) | 5.2027(1) | 18.39 | 4.07 | – |
| 0.25 | 3.2535(1) | 5.2037(1) | 14.35 | 4.21 | 2.7(2) |
| 0.30 | 3.2535(1) | 5.2036(1) | 17.39 | 2.12 | 13.7(3) |
| 0.35 | 3.2546(2) | 5.2051(1) | 7.76 | 2.61 | 19.0(2) |
| 0.50 | 3.2543(1) | 5.2053(1) | 4.80 | 2.08 | 45.9(4) |

**Table 2**
The Zn, O and Co occupation factors obtained by the Rietveld refinement for the wurtzite (W) $Zn_{1-x}Co_xO$ samples and rocksalt (R) $Co_{0.77}Zn_{0.23}O$ segregated phase. The $x_E$ and $y$ parameters are the effective Co and Zn concentrations measured by EDS, respectively.

| $x_N$ | Phase | Zn | O | Co | $x_E$ | $y$ |
|---|---|---|---|---|---|---|
| 0.15 | W | 0.855(6) | 1.008(9) | 0.145(6) | 0.164(6) | – |
| 0.20 | W | 0.79(1) | 1.005(7) | 0.22(1) | 0.208(4) | – |
| 0.25 | W | 0.758(1) | 0.998(1) | 0.230(1) | 0.226(4) | – |
| | R | 0.24(2) | 1.01(9) | 0.77(3) | – | 0.236(6) |
| 0.30 | W | 0.762(1) | 0.992(1) | 0.222(1) | 0.228(4) | – |
| | R | 0.231(5) | 0.982(2) | 0.769(8) | – | 0.234(2) |
| 0.35 | W | 0.767(1) | 1.051(8) | 0.226(2) | 0.229(4) | – |
| | R | 0.228(3) | 0.98(1) | 0.766(4) | – | 0.232(4) |
| 0.50 | W | 0.766(2) | 1.088(9) | 0.225(2) | 0.231(4) | – |
| | R | 0.228(2) | 1.008(8) | 0.767(2) | – | 0.234(6) |

In addition, the percentage of the $Co_{0.77}Zn_{0.23}O$ segregated phase ($n^{RS}$) is estimated by using the Rietveld refinement and is presented in Table 1. We quantitatively observed that increasing the $x_N$ corresponded with an increase in the $n^{RS}$. After reaching the solubility limit and while considering the constants of the molar masses of the wurtzite effective phase ($Zn_{0.77}Co_{0.23}O$, $M_E^W = 70.896\ \mathrm{g\ mol^{-1}}$) and the segregated phase ($Co_{0.77}Zn_{0.23}O$, $M_E^R = 76.415\ \mathrm{g\ mol^{-1}}$), the molar fraction of the segregated phases ($n_A^{RS}$) can be analytically calculated as follows:

$$n_A^{RS} = \frac{M_N^W - M_E^W}{M_E^R - M_E^W} \tag{1}$$

where $M_N^W$ is the molar mass correspondent to the nominal stoichiometry of the samples. The calculated values for $n_A^{RS}$ and $n^{RS}$ that were obtained through the Rietveld refinement (Table 1) are presented in Fig. 1(f). These values agree very well. Therefore, the combined use of XRD and SEM/EDS in this work indicates that it is possible to predict the relative percentages of the rocksalt $Co_{0.77}Zn_{0.23}O$ segregated phase and the Co-doped wurtzite ZnO phase when the nominal composition is greater than the Co solubility limit in the ZnO matrix. The coexistence of the wurtzite and the rocksalt phase is expected to occur for Co contents of less than 77%. Above 77%, a single cubic phase is expected to occur, as shown in Fig. 2(b). An XRD diffraction pattern of a $Co_{0.8}Zn_{0.2}O$ reference sample that was prepared under the same conditions as the $Zn_{1-x}Co_xO$ samples only corresponds to the rock-salt CoO structure, with no indication of the presence of wurtzite ZnO phase.

### 3.3. Raman scattering spectroscopy

To perform a detailed analysis of the chemical composition of the samples, Raman spectral mappings of the polished sample surfaces were acquired. At the $\Gamma$-point of the Brillouin zone (BZ) of the hexagonal wurtzite ZnO, the optical phonons are represented by $\Gamma = A_1 + 2B_1 + E_1 + 2E_2$. Here, $A_1$ and $B_1$ are one-dimensional modes, while $E_1$ and $E_2$ are two-dimensional modes. The two polar $A_1$ and $E_1$ modes and the two nonpolar $E_2$ modes are Raman active, while the two $B_1$ modes are inactive (silent modes). Thus, the $E_1$ and $A_1$ modes are divided into transverse optical (TO) and longitudinal optical (LO) phonons. The $E_2$ mode appears at two frequencies. The high-frequency mode is called $E_{2H}$, while the low-frequency mode is called $E_{2L}$. These modes are related to the vibrations of the oxygen and zinc sublattices, respectively.

Fig. 3(a), (c), (e) and (g) present the micrographs of the sample surfaces (different colored areas correspond to regions were distinct Raman spectra were acquired). In Fig. 3(b), (d), (f) and (h), we present the obtained spectra for the Co-doped ZnO matrix ($Zn_{1-x}Co_xO$) of the four samples at points 1, 3, 5, 6, 7 and 8 in the micrographs. In addition, the spectra for segregated phase ($Co_{0.77}Zn_{0.23}O$) is presented for points 2 and 4 of the samples with $x_N = 0.25$ and 0.30. The spectra for the Co-doped ZnO matrix were normalized by the amplitude of the $E_{2H}$ mode. The spectrum obtained for the $Co_{0.77}Zn_{0.23}O$ segregated phase did not resemble the Raman spectrum acquired for the pure CoO (Sigma–Aldrich, 99.99%) reference sample (Fig. 3(b)). This difference was associated with the incorporation of Zn into the CoO matrix and was pointed out by the EDS measurements. To address this point, the Raman spectrum of a $Co_{0.8}Zn_{0.2}O$ reference sample are presented in Fig. 3(d) and are superimposed on the spectrum obtained for the $Co_{0.77}Zn_{0.23}O$ segregated phase. The similarities between the spectra confirm the assumption of Zn incorporation into the CoO segregated phase.

In the areas corresponding to the $Zn_{1-x}Co_xO$ phase, we identified three main modes of ZnO, at 330, 380 and 437 $cm^{-1}$. These modes corresponded to the density of states of $2E_{2L}$ at the *M*-point of the BZ [34], and the $A_1(TO)$ and $E_{2H}$ modes, respectively. The presence of the main vibrational modes of ZnO confirmed that the hexagonal wurtzite structure occurred in all of the samples. In addition, a broad band at approximately 500–600 $cm^{-1}$ was observed that appeared to form from the overlapping of several peaks, with the most prominent peaks centered at 544 and 574 $cm^{-1}$. The peak at 574 $cm^{-1}$ could be assigned to the $A_1(LO)$ and $E_1(LO)$ phonon modes, which are very similar in energy. The peak at 544 $cm^{-1}$ can be assigned to the density of states correspondent to the $2A_1(LA)$ in the *M*–*K* direction of the BZ [34,35]. Generally, the pure ZnO $A_1(LO)$ and $E_1(LO)$ modes are less intense due to destructive interference between the potential deformation and Fröhlich interaction [36]. Nevertheless, the crystalline disorder induced by the incorporation of dopants, impurities, and defects can amplify these modes due to the consequential breakdown of the selection rules. Similar results have been observed in different systems and are generally assigned to complexes that involve intrinsic defects, such as oxygen vacancies ($V_O$) and interstitial zinc ($Zn_i$) [37]. The presence of these modes clearly indicates the presence of Co in our samples and is associated with the structural defects introduced by doping. These observed modes indicate the incorporation of Co into the ZnO matrix. As the cobalt concentration increases, the relative intensities of these defect-related modes to the main $E_{2H}$ mode also increase [38]. In Fig. 3(f) and (h), the relative intensities of the $2A_1(LA)$ density of states and the LO modes for the areas indicated by numbers 6 and 8 (brown areas in Fig. 3(e) and (g)) are greater than the intensities for the areas indicated by numbers 5 and 7 (yellow areas in Fig. 3(e) and (g)). This result indicates that the Co content is higher in these areas and reveals that this technique is sensitive enough to account for compositional inhomogeneities in the Co-doped ZnO matrix.

### 3.4. X-ray absorption

The structures of the $Zn_{1-x}Co_xO$ samples were also characterized using XAS measurements. X-ray Absorption Near-Edge Structure (XANES) spectra provide information regarding the coordination symmetry and the valence of ions incorporated into a solid. The energy of the absorption edge shifts according to the valence of the absorbing ion because the binding energy of the bound electrons increases as the valence increases. Additionally, the shape of the absorption edge depends on the unfilled local density of states and on the coordination symmetry of the absorbing element.

The spectrum at the Co *K*-edge is characteristic of the electron transition from the 1*s* state to the empty 4*p* states [39]. The pre-edge region is associated with the transitions of electrons from the 1*s* to 3*d* states. Although this transition is originally forbidden, it occurs due to the hybridization of the Co 3*d* states with O 2*p* in the sites without an inversion center of symmetry [39]. Fig. 4(a) shows the Co *K*-edge XANES spectra obtained for the $Zn_{1-x}Co_xO$ samples at room temperature. The spectra obtained for the samples with $x_N = 0.15$ and 0.20 have similar features, except for small differences in the white line intensity relative to the peak intensity in the pre-edge regions (inset of Fig. 4(a)). This observation indicates that no significant structural distortion occurs around the $Co^{2+}$ ions at different doping levels under the Co solubility limit (23%). Generally, the intensity of the pre-edge peak increases linearly with the substitutional incorporation of a TM into a solid due to the progressive participation of the 3*d* orbital in bonding [40]. For samples with $x_N = 0.25$ and 0.30, the shape of the spectra differs from the spectra observed for the samples with no segregated phase and approaches the spectrum obtained for the CoO reference sample. This result agrees with previous analyses. In addition, a relatively intense peak occurs in the pre-edge region for all samples. What would be expected considering the $Co^{2+}$ ions located in tetrahedral sites, which do not have an inversion center of symmetry. This result let us to conclude that the $Co^{2+}$ ions in our samples are replacing the $Zn^{2+}$ ions into the ZnO wurtzite structure [41].

The valence of the dopant ions can be analyzed by comparing their resulting edge structures with those obtained for the reference samples. In Fig. 4(a), we present the XANES spectra for Co ions and oxides with various metal oxidation states. The comparison with the spectra of our samples indicates that Co assumes predominantly the 2+ oxidation state.

Fig. 4(b) shows the modulus of the $k^3$ weighted Fourier transform that was extracted from the Co *K*-edge spectra for the $Zn_{1-x}Co_xO$ samples, a Co foil and the Co oxides powders. In addition, Fig. 4(b) shows the results obtained at the Zn *K*-edge for a pure ZnO reference sample prepared under the same conditions as the doped samples. We observed that the EXAFS data for the Co-doped samples with $x_N = 0.15$ and 0.20 were very similar and were different from those with $x_N = 0.25$ and 0.30 and from the Co foil and the Co oxides. In contrast, we observed that the EXAFS data were comparable to the data obtained from the Zn *K*-edge of pure ZnO. This result clearly indicates that the Co is located in the same environment as the Zn atoms in the ZnO host matrix.

The short-range structural data provided by EXAFS offers element-specific insights and provides quantitative information regarding the number, position and identity of atoms surrounding the absorbing element and the structural disorder within the coordination spheres. To obtain quantitative information regarding the local structure around the Co atoms, Fourier transform curves were back-Fourier transformed between 1.5 and 3.5 Å to obtain the experimental EXAFS spectra that were fit using a theoretical model that was calculated by using the FEFF9 code and the crystallographic information according to the XRD measurements.

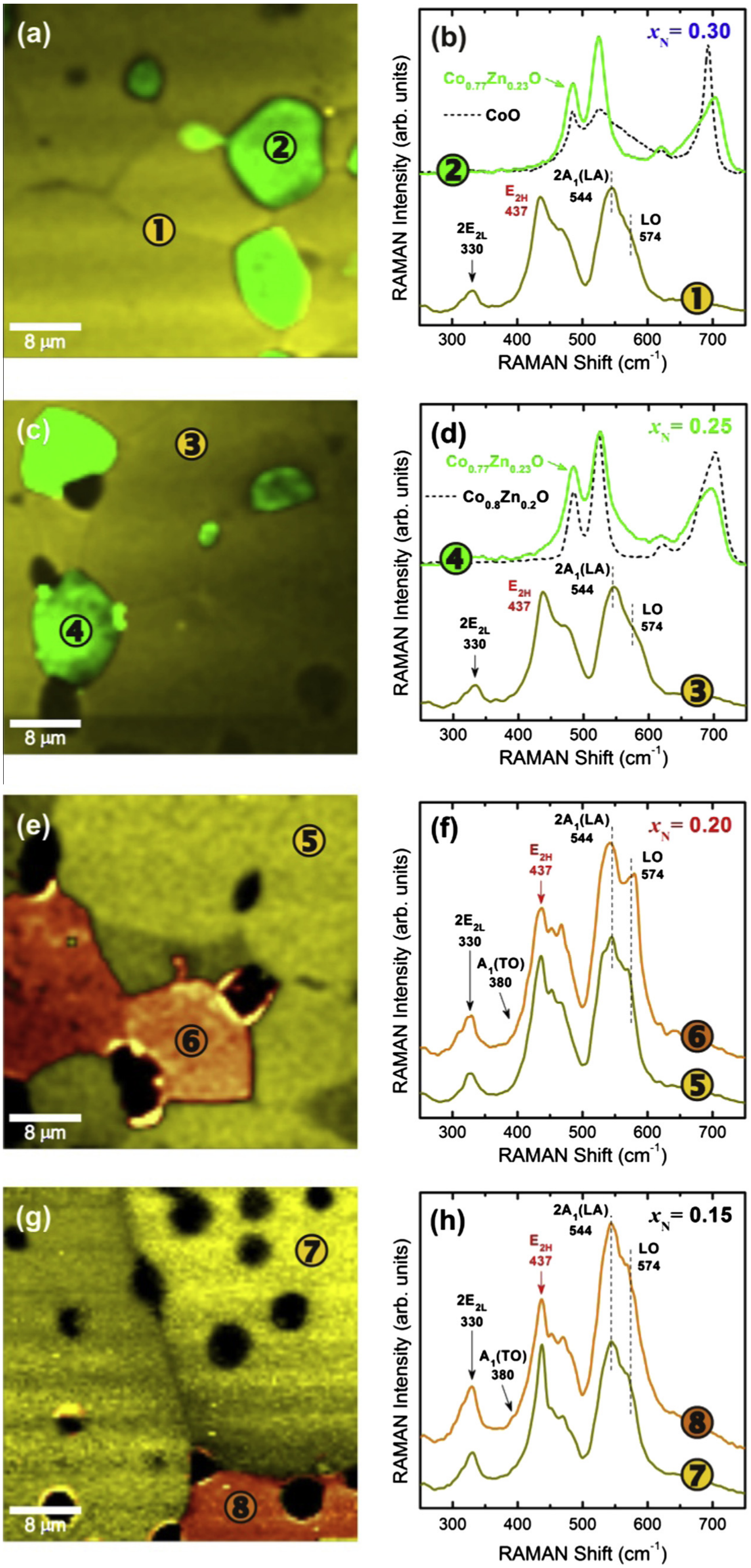

**Fig. 3.** (a), (c), (e) and (g) Micrographs of the surfaces of the $Zn_{1-x}Co_xO$ samples with $x_N$ = 0.30, 0.25, 0.20 and 0.15, respectively, indicating (colors) where the Raman spectra were measured. (b), (d), (f) and (h) contain the Raman spectra for the different places identified in (a), (c), (e) and (g). The black dashed line in (b) and (d) indicate the spectra obtained for the reference samples CoO and $Co_{0.8}Zn_{0.2}O$, respectively. (For interpretation of the references to color in this figure legend, the reader is referred to the web version of this article.)

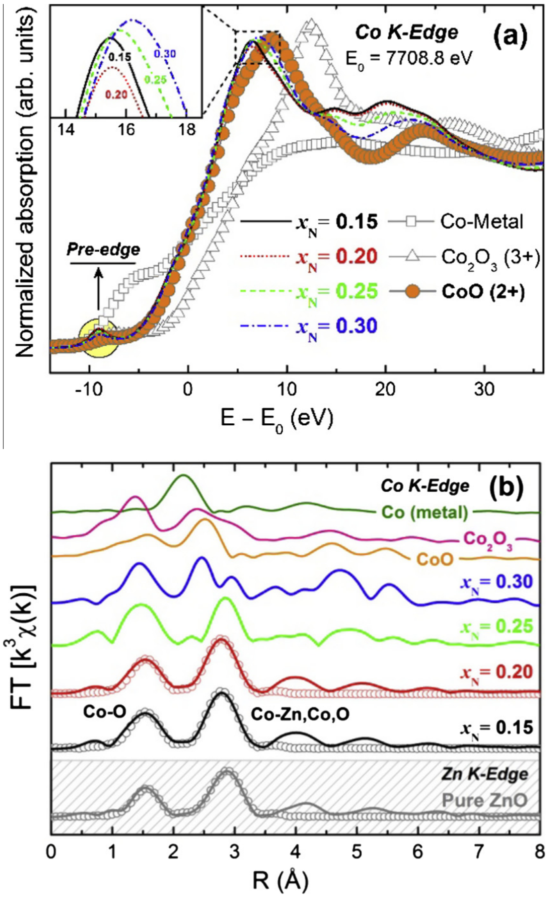

**Fig. 4.** (a) Co *K*-edge XANES spectra for the $Zn_{1-x}Co_xO$ samples. Spectra of metallic Co, rock-salt CoO (oxidation state of 2+) and $Co_2O_3$ (oxidation state of 3+) are also shown for comparison. The inset highlights the white line peak. (b) EXAFS data: modulus of $k^3$ weighted Fourier transforms of Co and Zn *K*-edge data from the bulk samples and reference powders. Solid lines are the experimental data and the open symbols represent the fits using the parameters shown in Table 3.

Because of the observed CoO secondary phase, the fits were only performed for samples with $x_N = 0.15$ and 0.20 and pure ZnO, whose fitted $k^3$ weighted Fourier transforms are shown in Fig. 4(b). In all fits, we considered single and multi-scattering paths that corresponded to four successive atomic shells around the Co placed at the Zn in the ZnO host matrix according to hexagonal wurtzite with a space group of $P6_3mc$. The number of free parameters was smaller than the number of independent points, which was defined as $N_{ind} = 2\Delta R\Delta k/\pi$, where $\Delta R$ is the width of the *R*-space filter windows, and $\Delta k$ is the actual interval of the fit in *k*-space [42]. The reliability of the fit, which was determined from the quality factor (*Q*) [42], coordination number (*N*), interatomic distances (*R*) and Debye–Waller factor ($\sigma^2$) relative to the fits are shown in Table 3. According to the structural model, the more intense peak between 1.0 and 2.0 Å in the Fourier transform spectra of the $Zn_{1-x}Co_xO$ samples corresponds to a single scattering interaction between the first O atoms around the absorber atom. Relative to the Co–Co and Co–O (beyond the first O neighbors) paths, the single scattering interactions correspond to the peaks and shoulders observed between 2.5 and 3.5 Å. This region also includes multiple scattering path interactions, such as Co–O–O, Co–O–Zn–O, Co–O–O–O and Co–Zn–O. As shown in Table 3, the obtained *Q* factors indicate the reliability of the fits, which are confirmed by the match between the fit (symbols) and experimental (lines) spectra shown in Fig. 4(b). The average coordination number for the Co–O interaction is constant within the experimental uncertainty. The good agreement between the experimental and fitted data confirms the substitutional character of Co doping of the ZnO matrix in the samples with $x_N = 0.15$ and 0.20.

**Table 3**
Results from the fits of the EXAFS spectra of the Co *K*-edge. EXAFS simulation were obtained by assuming that Co placed at the Zn site in the ZnO matrix for the single phase $Zn_{1-x}Co_xO$ and for the ZnO reference samples. Here, *R* is the distance from the central atom, *N* is the average coordination number, $\sigma^2$ the Debye–Waller factor and *Q* is the quality factor.

| Sample | Shell | *R* (Å) | N | $\sigma^2$ (Å$^2$) | Q |
|---|---|---|---|---|---|
| Pure ZnO | Zn–O | 1.96(1) | 4.4(4) | 0.004(1) | 1.36 |
| | Zn–Zn | 3.22(1) | 8.7(7) | 0.0055(5) | |
| | Zn–Zn | 3.19(2) | 5.0(1.5) | 0.0055(5) | |
| | Zn–O | 3.86(2) | 8.0(2.5) | 0.004(1) | |
| $x_N = 0.15$ | Co–O | 1.98(1) | 4.6(5) | 0.004(1) | 2.22 |
| | Co–Zn | 3.22(1) | 7.0(1.0) | 0.005(1) | |
| | Co–Zn | 3.19(2) | 4.4(8) | 0.005(1) | |
| | Co–O | 3.86(2) | 8.0(1.6) | 0.004(1) | |
| $x_N = 0.20$ | Co–O | 1.98(1) | 4.5(5) | 0.004(1) | 1.69 |
| | Co–Zn | 3.21(2) | 6.0(2.8) | 0.005(1) | |
| | Co–Zn | 3.21(3) | 4.0(3.0) | 0.005(1) | |
| | Co–O | 3.86(2) | 8.0(1.6) | 0.004(1) | |

In summary, the structural analysis confirms that the $Co^{2+}$ ions occupy the Zn-sites of the ZnO wurtzite structure in the $Zn_{1-x}Co_xO$ samples with $x_N = 0.15$ and 0.20. Clearly, for these samples, the results exclude the presence of magnetic extrinsic sources, such as Co-rich nanocrystals or segregated secondary magnetic phases. For the samples with $x_N = 0.25$ and 0.30, Co solubility is achieved and a Zn-doped CoO phase, $Co_{1-x}Zn_xO$, is segregated. With these considerations, we proceed to magnetic characterization.

### 3.5. Magnetometry

The magnetization (*M*) of the samples measured as a function of the magnetic field (*H*) at *T* = 300 K is displayed in Fig. 5(a). The results are consistent with typical paramagnetic behavior ($M = \chi H$). In this case, no ferromagnetic component was observed. Fig. 5(b) shows the inverse of the *dc* magnetic susceptibility as a function of temperature for the four studied samples. The displayed data were obtained by measuring the magnetization at low magnetic fields (*H* = 0.1 T) and include a small correction from the diamagnetic contribution of the ZnO lattice. For the samples with $x_N = 0.15$ and $x_N = 0.20$, the susceptibility data display a Curie–Weiss (CW) behavior in the high temperature range of 100–300 K that is characterized by a large and negative CW temperature. Below 100 K, the magnetic susceptibility departs from the CW law in the form of a downturn in the graph of the inverse susceptibility versus temperature. The present overall features of the susceptibility data for these two samples are usually obtained for II–VI based DMS [43,44] and are characterized as a paramagnetic phase with a large antiferromagnetic (AF) exchange interaction between neighboring $Co^{2+}$ ions. For the samples with $x_N = 0.25$ and 0.30, deviations from the CW law are observed in the form of a broad cusp centered near 220 K (inset of Fig. 5(b)), which is more pronounced for the $x_N = 0.30$ sample and was attributed to the AF transition of the $Co_{1-x}Zn_xO$ phase that was determined in the previous section [45].

The susceptibility data for $x_N = 0.15$ and 0.20 were fit in the high temperature range using the following CW law: $\chi(T) = C/(T - \theta)$, where *C* is the Curie constant and $\theta$ is the CW temperature. The Curie constant is related to the $Co^{2+}$ concentration $x_M$ as follows: $C = Nx_M(g\mu_B)^2S(S+1)/3k_B$. Here, *N* is the total number of cations per gram, and *g* and *S* are the effective Landé factor and the spin of the $Co^{2+}$ ions, respectively ($g = 2.264$, $S = 3/2$) [46,47]. For the samples with nominal concentrations of $x_N = 0.15$ and 0.20, we

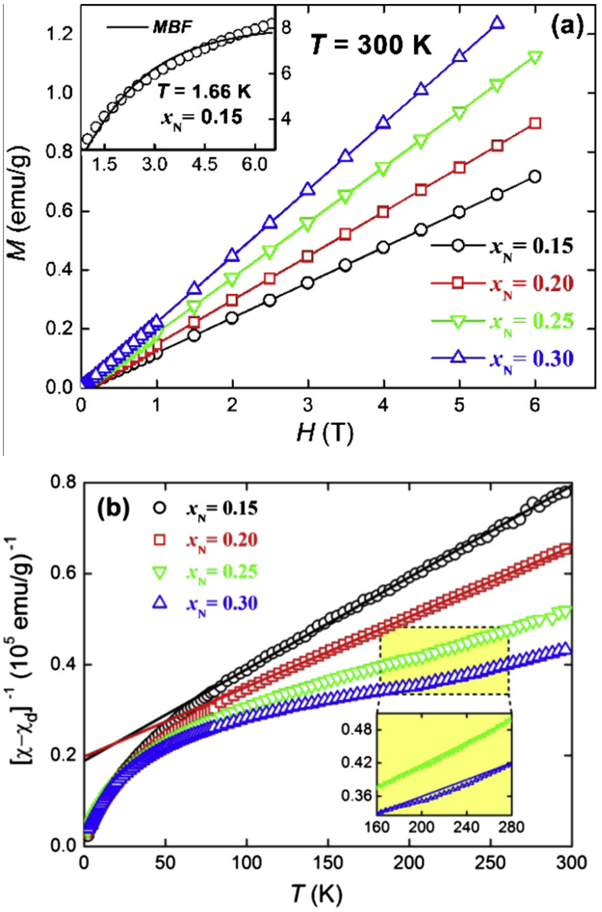

**Fig. 5.** (a) $M(H)$ curves for the $Zn_{1-x}Co_xO$ samples at 300 K. The inset presents the $M(H)$ curve for the sample with $x = 0.15$ at 1.66 K. The symbols are the experimental data, and the line is the fit generated using a modified Brillouin function (MBF). (b) Inverse *dc* magnetic susceptibility $\chi$ versus temperature for the $Zn_{1-x}Co_xO$ samples. The best fit of the high-temperature data to the Curie–Weiss law is shown as a solid line.

obtained $x_M = 0.166$ and $x_M = 0.216$, respectively. The obtained values of the CW temperature were −95 K for the sample with $x_N = 0.15$ and −128 K for the sample with $x_N = 0.20$. From this result, we determined that $\theta_0 = \theta/x_M = -582 \pm 10$ K (which corresponds to an exchange constant $J_1 = -19.4 \pm 0.3$ K). These values agree with our previous results [38] and the results of other works [48–50].

Regarding the bound magnetic polaron (BMP) model, a long-range magnetic order occurs in a truly dilute magnetic semiconductor when two conditions are satisfied. First, the dopant concentration ($x$) must be lower than the dopant percolation threshold ($x_P$) and homogeneous throughout the sample volume. Second, the percentage of defects ($\delta$) must be larger than the polaron percolation threshold ($\delta_P$) to assure that all of the dopants will be ferromagnetically coupled. For the ZnO system, $\delta_P = 0.0015$ and $x_P = 0.18$ [18]. Regarding the samples with $x_N = 0.20$, 0.25 and 0.30, the Co concentrations are above the dopant percolation threshold ($x_N > x_P$) and our results from magnetic characterization are in accordance with the BMP model. For the sample with $x_N = 0.15$, which satisfies the first condition, the conventional paramagnetic phase with AF coupling between $Co^{2+}$ neighbors is obtained. To obtain more insight regarding the origins of this magnetic behavior, the magnetization data were obtained as a function of the magnetic field at $T = 1.66$ K for the sample with $x_N = 0.15$, as displayed in the inset of Fig. 5(a). The low temperature magnetization curve is not saturated at the highest applied magnetic field and cannot be fit by the modified Brillouin function (MBF) [51]. This behavior is mainly attributed to the effects of relatively large AF exchange interactions and, because the Co concentration in this sample is over 10% ($x_N = 0.15$), to the existence of large AF clusters [52]. This last point may be reinforced by considering that the substitution of Zn for Co may not be random. The tendency for $Co^{2+}$ ions to group together into the ZnO host matrix was reported from both experimental [26,53] and theoretical [54,55] perspectives and must be considered. The $Co^{2+}$ single-ion anisotropy [56,57] may also contribute to the observed lower magnetization value; however, due to the polycrystalline character of our samples, its effect may be relatively weak. The measured magnetization value for the high field ($M(6.5\ \text{T}) = 8.2$ emu/g) was much lower than the expected saturation value of the magnetization ($M_0 = 39.2$ emu/g) for $x_M = 0.166$. This result was also observed for other II–VI based DMS [52]. The obtained ratio of $M(6.5\ \text{T})/M_0 = 0.21$ agrees with previous experimental results [44,48,58] and indicates that approximately 21% of the magnetic moments are not in a fully compensated AF configuration. This fraction corresponds to an effective magnetic moment concentration of approximately 3%, which agrees with the results obtained by Ney et al. [57] for a sample with a Co concentration of 15% considering singles (isolated $Co^{2+}$ ions without a second Co ion in the next-cation neighbor shell) and open triplets (open Co–O–Co–O–Co clustered configuration) as the dominant Co configurations that contribute to the measured magnetization. Again, according to the scope of the BMP model, these non-compensated moments could be FM coupled through polarons. Once the FM coupling was not observed, we inferred that the density of defects in our samples was below the polaron percolation threshold ($\delta < \delta_P \cong 0.15\%$ for the ZnO matrix). In fact, based on the experimental techniques used in this work, we were unable to directly measure the densities of defects present in our samples, likely due to their small values. Therefore, based on the BMP model, a purely paramagnetic behavior was expected and was observe.

### 3.6. Monte Carlo simulation

The theoretical simulation of the magnetic properties for semiconductors doped with transition metals (DMSs) involves knowledge regarding the cluster types and its probabilities. For doping concentrations of more than 10%, these calculations were not accurate due to the lack of the cluster statistics. To qualitatively address the role of the exchange interactions between the localized $Co^{2+}$ magnetic moments in the ZnO matrix, a sequence of Monte Carlo (MC) simulations was performed, using classical spins in the Heisenberg $J_1$–$J_2$ model described by [59]

$$\widehat{H} = J_1^{\text{in}} \sum_{[i;j]} S_i \cdot S_j + J_1^{\text{out}} \sum_{\langle i;j \rangle} S_i \cdot S_j + J_2 \sum_{(i;j)} S_i \cdot S_j + D \sum_j S_{z;j}^2 + g\mu_B \sum_j H \cdot S_j \qquad (2)$$

where $[i;j]$, $\langle i;j \rangle$, and $(i;j)$ are the sums of the in-plane, out-plane, and second neighbor pairs, respectively, $J_1^{\text{in}}$ is the in-plane coupling, $J_1^{\text{out}}$ is the out plane coupling, $J_2$ is the second neighbor coupling and $D$ is the single ion anisotropy constant, which corresponds to the Zeeman interaction.

We tested five different sets of magnetic parameters (Table 4). Set I considers an isotropic system with a week exchange coupling between the magnetic ions. Set II also considers an isotropic system with exchange coupling that corresponds to that measured for our samples ($J_1 = -19.4 \pm 0.3$ K). Set III introduces the anisotropy regarding the ZnO wurtzite structure [60] and includes the exchange coupling related to distant neighbors (DN) up to $J_2$. The values were extracted from the work performed by D'Ambrosio

**Table 4**
Set of magnetic parameters used in the MC simulations.

| Set | $J_1^{in}$ (K) | $J_1^{out}$ (K) | $J_2$ (K) | $D$ (meV) | Cobalt distribution |
|---|---|---|---|---|---|
| I | −2 | −2 | 0 | 0 | Random |
| II | −19.4 | −19.4 | 0 | 0 | Random |
| III | −25.6 | −8.5 | −1.1 | 0 | Random |
| IV | −25.6 | −8.5 | −1.1 | 0.342 | Random |
| V | −25.6 | −8.5 | −1.1 | 0.342 | Clustered |

et al. [61], $J^{(3)}$ was assumed to be equal to $J_2$, once considering it as the second-largest exchange constant based on theoretical assumptions [62–64]. Set IV is the same as set III, but the single-ion anisotropy was counted with $D = 0.342$ meV [46]. In all previous arrangements, the samples were formed by a random distribution of $Co^{2+}$ ions in the Zn sites with a molar Co concentration of up to 15%. Set V is the same as set IV, but considers clusters (non-random distribution) of the $Co^{2+}$ ions over the sample volume. The clustered samples were formed in two steps. First, a sample with a Co concentration of 2% was randomly distributed throughout the sample volume. Next, further distribution of the remaining Co atoms around the initial Co atoms was conducted based on a heuristic acceptance probability of 0.005%, until the Co concentration reached 15%. This model makes it possible to form Co rich regions with random shapes.

The MC procedure began with a sample formation that distributed Co ions over the ZnO matrix and calculated the energy of each site. The samples were prepared to have approximately 6500 magnetic sites. We adopted a slowdown cooling process with the Metropolis algorithm applied to the energy acceptance. The MC process used $1.5 \times 10^6$ MC steps, and the thermal average of the parameters was calculate in $10^4$ steps. The final presented results corresponded to an average of over 20 different samples. Boundary periodic conditions were adopted in all simulations. After the thermal equilibrium is reached, the Edwards–Anderson order parameter ($q_{EA}$), the specific heat ($c_V$), and the magnetization ($M$) normalized by the saturation magnetization ($M_S$) versus the external magnetic field ($H$) were calculated. The $q_{EA}$ order parameter is defined as [65]

$$q_{EA} = \frac{1}{N}\sum_{i=1}^{N}\left(\sum_{\alpha}\left|\frac{1}{t}\sum_{t'=t_0}^{t_0+t} S_{i;\alpha}\right|^2\right)^{1/2} \tag{3}$$

where $\alpha = x$, $y$ and $z$. To avoid spurious results when obtaining an average over a large time interval $t$, the summation was performed by starting at a time $t_0$ that corresponded to the thermal equilibrium of the system. The specific heat was calculated based on thermal fluctuations. The $M(H)$ curves were obtained by using the metropolis algorithm for the interaction energy, as given by Eq. (2). To qualitatively reproduce the $M(H)$ curves measured for our polycrystalline samples, we present the normalized magnetization averaged over the external magnetic field applied from the parallel to the perpendicular direction of the $c$-axis ($z$ direction) of the ZnO wurtzite structure ($M_{avg}/M_S$).

Fig. 6 shows the MC results. Fig. 6(a) presents the $q_{EA}$ order parameter and the $c_V$ as a function of the temperature. Except for set I (the isotropic case with lower exchange coupling), all of the curves present behavior that is typical of the transition from a random oriented set of moments at higher temperatures to an ordered system with antiferromagnetically coupled moments at lower temperatures. This behavior is evidenced by the $c_V$ curves (inset of Fig. 6(a)), which presents a maximum at a critical temperature were the transition between the two conditions occurs [65,66]. We observed few differences between the curves for sets II and III. This result can be explained, regarding the simulations, by considering the relative lower number of coupled neighbors by $J_2$ compared with those coupled by $J_1^{in}$ and $J_1^{out}$. By introducing the single-ion anisotropy in set IV, the transition becomes more evident in both $q_{EA}$ and $c_V$ curves. The single-ion anisotropy of the form of $DS_z^2$ correspond to a ground state and is associated with the lowest $S_z$, meaning that the spins tend to stay near the plane that is perpendicular to $z$. This trend can observed as an easy magnetization plane in which the spins are more energetically favorable for alignment during cooling [45,59]. For set V (the clustered system) the transition is even more pronounced and occurs at higher temperatures. In a clustered system, the average distance between the $Co^{2+}$ ions is shorter, which results in an increase in the number of magnetic coupled ions, favoring the order against the thermally induced disorder.

Fig. 6(b) presents the $M_{avg}/M_S$ versus $H$ calculated at 2 K. The obtained curve for set I was fit well by the Brillouin Function (BF), which highlights the pure paramagnetic character of this system, even at low temperatures. For all of the other curves, we observed a departure from the last scenario that was comparable to those of the $M(H)$ curves experimentally observed for different DMSs [52]. Here, the curve corresponding to set III was only slightly different from that observed for set II. The magnetization increases quickly at low fields due to the alignment of the singles, and a ramp is observed in the sequence that is mainly associated with the pairs. As previously shown, due to the random crystalline orientation of a polycrystalline samples with respect to the direction of the applied magnetic field, the single-ion anisotropy (set IV) only introduces a small departure from the previous sets. Finally, for the clustered system (set V), the fast increase associated with the singles is less pronounced and the ramp that is mainly associated with the pairs is larger. This result is expected in a

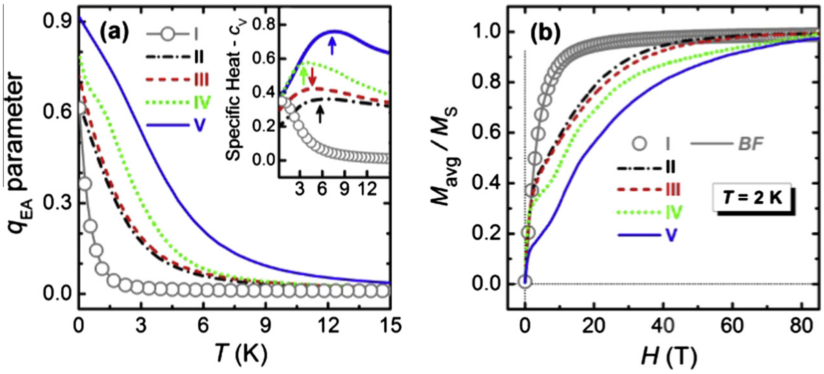

**Fig. 6.** (a) Calculated $q_{EA}$ parameter and the specific heat ($c_V$) (inset) as a function of the temperature. (b) $M_{avg}/M_S$ vesus $H$ curves calculated at 2 K. The values of the magnetic parameters used for each set are presented in Table 4. The curve associated with set I is fit by a Brillouin Function (BF).

scenario were the $Co^{2+}$ ions are bunched together [67]. Although we used a very small heuristic acceptance probability to distribute $Co^{2+}$ ions around already placed Co in the ZnO structure, only 0.005%, the obtained curve shows a considerable difference relative to the ones for the previous sets. The oscillations present in the magnetization curves for sets IV and V mainly resulted from the introduction of the anisotropic term ($D$) in the Hamiltonian. The results of the MC simulation confirmed our previous assumptions that the departure of the observed magnetization, at low temperature, from the MBF for the sample with $x_N = 0.15$ was mainly due to relatively large AF exchange interactions and the existence of large AF clusters. However, we likely overestimated the value of the single-ion anisotropy constant ($D$) in our calculation. Ney et al. [57] also indicated that the $D$ value decreased as the Co concentration increased. Specifically, for a Co concentration of 15%, these authors observed a $D$ value of approximately 2 K. Finally, for the samples with relatively higher Co concentrations, the distant neighbor exchange constants ($J_2$, $J_3$, etc.) could present different values from those measured by D'Ambrosio et al. [61]. The values of the exchange interaction could be higher, which could lead to more pronounced differences between sets II and III.

## 4. Conclusions

We have presented an extensive microstructure and magnetic analysis of bulk $Zn_{1-x}Co_xO$ samples that were prepared using the solid-state reaction method. Structural characterization revealed that the $Zn_{1-x}Co_xO$ ceramic samples with $x_N = 0.15$ and 0.20 were free of secondary phases, whereas samples with $x_N = 0.25$ and 0.30 exhibited a segregated phase that was identified as $Co_{1-y}Zn_yO$ with $y = 0.23$. The solubility of the $Co^{2+}$ ions was determined as approximately 23% in the ZnO matrix at a sintering temperature of 1400 °C. Our results show that it is possible to predict the relative percentage of doped wurtzite ZnO and rock-salt CoO in samples prepared with nominal compositions between $0.23 \leqslant x \leqslant 0.77$. The magnetic characterization of the samples reveals conventional paramagnetic behavior with large AF coupling of $Co^{2+}$ ions. The obtained values of the CW temperature were −95 K for the sample with $x_N = 0.15$ and −128 K for the sample with $x_N = 0.20$. From this result, we determined that the $Co^{2+}$ exchange coupling constant in those samples is of $J_1 = -19.4 \pm 0.3$ K. Specially, from the magnetic results of the sample with $x_N = 0.15$, the MC simulation led to the conclusion that the departure of the $M(H)$ from the MBF mainly resulted from the relative large AF exchange interactions and the existence of large AF clusters. In addition, magnetic characterization supported the finding that a considerable fraction of the magnetic moments (21%) remains in the non-compensated configuration. Under these conditions and by invoking the BMP model, we inferred that the ferromagnetic behavior is not observed due to the low density of defects in the sample, despite the incorporation of $Co^{2+}$ ions in the ZnO matrix.

## Acknowledgements

We gratefully acknowledge support from the following agencies: FAPEMIG (APQ-02600-12 and PPM-00524-12), CNPq (476870/2011-9), CAPES (PNPD-2011), FINEP (Ref. 134/08), MINECO (MAT2012-33483) and FAPESP. We also thank CNPq and CAPES for providing research fellowships (ACD, AOZ and AM). Furthermore, the authors also acknowledge LNLS for the XAS measurements and Prof. Dr. F. Iikawa and Profa. Dra. M.J.S. at the Universidade de Campinas of Brazil (UNICAMP) for the Raman measurements. The authors acknowledge Dr. Said Agouram for providing support for the HRTEM measurements.

## References

[1] F. Pan, C. Song, X.J. Liu, Y.C. Yang, F. Zeng, Mater. Sci. Eng. R: Rep. 62 (2008) 1.
[2] S. Lee, Y. Shon, S.W. Lee, S.J. Hwang, H.S. Lee, T.W. Kang, D.Y. Kim, Appl. Phys. Lett. 88 (2006) 212513.
[3] S.J. Lee, H.S. Lee, D.Y. Kim, T.W. Kim, J. Cryst. Growth 276 (2005) 1217.
[4] G. Schmidt, D. Ferrand, L.W. Molenkamp, A.T. Filip, B.J. van Wees, Phys. Rev. B 62 (2000) R4790.
[5] R. Fiederling, M. Keim, G. Reuscher, W. Ossau, G. Schmidt, A. Waag, L.W. Molenkamp, Nature 402 (1999) 787.
[6] Y. Ohno, D.K. Young, B. Beschoten, F. Matsukura, H. Ohno, D.D. Awschalom, Nature 402 (1999) 790.
[7] D. Chiba, M. Yamanouchi, F. Matsukura, H. Ohno, Science 301 (2003) 943.
[8] H. Ohno, D. Chiba, F. Matsukura, T. Omiya, E. Abe, T. Dietl, Y. Ohno, K. Ohtani, Nature 408 (2000) 944.
[9] T. Dietl, H. Ohno, F. Matsukura, J. Cibert, D. Ferrand, Science 1019 (2000) 287.
[10] G. Martinez-Criado, O. Sancho-Juan, N. Garro, J.A. Sans, A. Cantarero, J. Susini, M. Roever, D.D. Mai, A. Bedoya-Pinto, J. Malindretos, A. Rizzi, Appl. Phys. Lett. 93 (2008) 021916.
[11] S. Venkataraj, N. Ohashi, I. Sakaguchi, Y. Adachi, T. Ohgaki, H. Ryoken, H. Haneda, J. Appl. Phys. 102 (2007) 014905.
[12] S. Kolesnik, B. Dabrowski, J. Mais, J. Appl. Phys. 95 (2004) 2582.
[13] D.C. Kundaliya, S.B. Ogale, S.E. Lofland, S. Dhar, C.J. Metting, S.R. Shinde, Z. Ma, B. Varughese, K.V. Ramanujachary, L. Salamanca-Riba, T. Venkatesan, Nat. Mater. 3 (2004) 709.
[14] T. Dietl, T. Andrearczyk, A. Lipinska, M. Kiecana, M. Tay, Y.H. Wu, Phys. Rev. B 76 (2007) 155312.
[15] Q. Xu, H. Schmidt, S. Zhou, K. Potzger, M. Helm, H. Hochmuth, M. Lorenz, A. Setzer, P. Esquinazi, C. Meinecke, M. Grundmann, Appl. Phys. Lett. 92 (2008) 082508.
[16] T. Fukumura, H. Toyosaki, Y. Yamada, Semicond. Sci. Technol. 20 (2005) S103.
[17] M.J. Calderon, S.D. Sarma, Ann. Phys. – New York 322 (2007) 2618.
[18] J.M.D. Coey, M. Venkatesan, C.B. Fitzgerald, Nat. Mater. 4 (2005) 173.
[19] J.M.D. Coey, K. Wongsaprom, J. Alaria, M. Venkatesan, J. Phys. D: Appl. Phys. 41 (2008) 134012.
[20] Y. Belghazi, G. Schmerber, S. Colis, J.L. Rehspringer, A. Dinia, Appl. Phys. Lett. 89 (2006) 122504.
[21] J.M.D. Coey, Curr. Opin. Solid State Mater. Sci. 10 (2006) 83.
[22] M. Tay, Y.H. Wu, G.C. Han, T.C. Chong, Y.K. Zheng, S.J. Wang, Y.B. Chen, X.Q. Pan, J. Appl. Phys. 100 (2006) 063910.
[23] V. Jayaram, B.S. Rani, Mater. Sci. Eng., A 304 (2001) 800.
[24] S.K. Mandal, A.K. Das, T.K. Nath, D. Karmakar, Appl. Phys. Lett. 89 (2006) 144105.
[25] B.B. Straumal, A.A. Mazilkin, S.G. Protasova, A.A. Myatiev, P.B. Straumal, B. Baretzky, Acta Mater. 56 (2008) 6246.
[26] B.B. Straumal, S.G. Protasova, A.A. Mazilkin, G. Schutz, E. Goering, B. Baretzky, P.B. Straumal, JETP Lett. 97 (2013) 367.
[27] N.H. Perry, T.O. Mason, J. Am. Ceram. Soc. 96 (2013) 966.
[28] A.C. Larson, R.B. Von Dreele, Los Alamos National Laboratory Report LAUR 86-7481994.
[29] B.H. Toby, J. Appl. Crystallogr. 34 (2001) 210.
[30] A. Michalowicz, J. Moscovici, D. Muller-Bouvet, K. Provost, J. Phys: Conf. Ser. 190 (2009) 012034.
[31] A.L. Ankudinov, B. Ravel, S.D. Conradson, J.J. Rehr, Phys. Rev. B 58 (1998) 7565.
[32] S.C. Abrahams, Jl. Bernstei, Acta Crystallogr., Sect. B: Struct. Sci. 25 (1969) 1233.
[33] S. Sasaki, K. Fujino, Y. Takeuchi, Pro. Jpn. Acad. Ser. B 55 (1979) 43.
[34] J.M. Calleja, M. Cardona, Phys. Rev. B 16 (1977) 3753.
[35] J. Serrano, A.H. Romero, F.J. Manjon, R. Lauck, M. Cardona, A. Rubio, Phys. Rev. B 69 (2004) 094306.
[36] R.H. Callender, S.S. Sussman, M. Selders, R.K. Chang, Phys. Rev. B 7 (1973) 3788.
[37] X. Wang, J. Xu, X. Yu, K. Xue, J. Yu, X. Zhao, Appl. Phys. Lett. 91 (2007) 031908.
[38] H.B. de Carvalho, M.P.F. de Godoy, R.W.D. Paes, M. Mir, A. Ortiz de Zevallos, F. Iikawa, M.J.S.P. Brasil, V.A. Chitta, W.B. Ferraz, M.A. Boselli, A.C.S. Sabioni, J. Appl. Phys. 108 (2010) 033914.
[39] Y. Orikasa, T. Ina, T. Nakao, A. Mineshige, K. Amezawa, M. Oishi, H. Arai, Z. Ogumi, Y. Uchimoto, J. Phys. Chem. C 115 (2011) 16433.
[40] W.F. Pong, R.A. Mayanovic, K.T. Wu, P.K. Tseng, B.A. Bunker, A. Hiraya, M. Watanabe, Phys. Rev. B 50 (1994) 7371.
[41] J. Pellicer-Porres, A. Segura, J.F. Sanchez-Royo, J.A. Sans, J.P. Itie, A.M. Flank, P. Lagarde, A. Polian, Superlattices Microstruct. 42 (2007) 251.
[42] S.S. Hasnain, Report on the International Workshops on Standards and Criteria in XAFS, in: X-ray Absorption Fine Structure: Proceedings of the VI International Conference on X-ray Absorption Fine Structures, Ellis Horwood New York, 1991.
[43] C.J. Chen, M. Qu, W. Hu, X. Zhang, F. Lin, H.B. Hu, K.J. Ma, W. Giriat, J. Appl. Phys. 69 (1991) 6114.
[44] S.W. Yoon, S.B. Cho, S.C. We, S. Yoon, B.J. Suh, H.K. Song, Y.J. Shin, J. Appl. Phys. 93 (2003) 7879.
[45] M.D. Rechtin, B.L. Averbach, Phys. Rev. B 6 (1972) 4294.
[46] P. Sati, R. Hayn, R. Kuzian, S. Regnier, S. Schafer, A. Stepanov, C. Morhain, C. Deparis, M. Laugt, M. Goiran, Z. Golacki, Phys. Rev. Lett. 96 (2006) 017203.
[47] N. Jedrecy, H.J. von Bardeleben, Y. Zheng, J.L. Cantin, Phys. Rev. B 69 (2004) 041308.

[48] S.J. Han, B.Y. Lee, J.S. Ku, Y.B. Kim, Y.H. Jeong, J. Magn. Magn. Mater. 2004 (2008) 272.

[49] S. Yin, M.X. Xu, L. Yang, J.F. Liu, H. Rosner, H. Hahn, H. Gleiter, D. Schild, S. Doyle, T. Liu, T.D. Hu, E. Takayama-Muromachi, J.Z. Jiang, Phys. Rev. B 73 (2006) 224408.

[50] L.B. Duan, W.G. Chu, J. Yu, Y.C. Wang, L.N. Zhang, G.Y. Liu, J.K. Liang, G.H. Rao, J. Magn. Magn. Mater. 320 (2008) 1573.

[51] T. Fukumura, Z.W. Jin, M. Kawasaki, T. Shono, T. Hasegawa, S. Koshihara, H. Koinuma, Appl. Phys. Lett. 78 (2001) 958.

[52] Y. Shapira, V. Bindilatti, J. Appl. Phys. 92 (2002) 4155.

[53] Y.B. Zhang, T. Sritharan, S. Li, Phys. Rev. B 73 (2006) 172404.

[54] N. Sanchez, S. Gallego, M.C. Munoz, Appl. Phys. Lett. 99 (2011) 153102.

[55] B. Sanyal, R. Knut, O. Granas, D.M. Iusan, O. Karis, O. Eriksson, J. Appl. Phys. 103 (2008) 07D131.

[56] P. Sati, C. Deparis, C. Morhain, S. Schafer, A. Stepanov, Phys. Rev. Lett. 98 (2007) 137204.

[57] A. Ney, T. Kammermeier, K. Ollefs, S. Ye, V. Ney, T.C. Kaspar, S.A. Chambers, F. Wilhelm, A. Rogalev, Phys. Rev. B 81 (2010) 054420.

[58] M. Bouloudenine, N. Viart, S. Colis, J. Kortus, A. Dinia, Appl. Phys. Lett. 87 (2005) 052501.

[59] P. Sati, S. Schafer, C. Morhain, C. Deparis, A. Stepanov, Superlattices Microstruct. 42 (2007) 191.

[60] T.Q. Vu, V. Bindilatti, Y. Shapira, E.J. Mcniff, C.C. Agosta, J. Papp, R. Kershaw, K. Dwight, A. Wold, Phys. Rev. B 46 (1992) 11617.

[61] S. D'Ambrosio, V. Pashchenko, J.M. Mignot, O. Ignatchik, R.O. Kuzian, A. Savoyant, Z. Golacki, K. Grasza, A. Stepanov, Phys. Rev. B 86 (2012) 035202.

[62] S.S. Yu, V.C. Lee, Phys. Rev. B 52 (1995) 4647.

[63] T.M. Rusin, Phys. Rev. B 53 (1996) 12577.

[64] A. Twardowski, H.J.M. Swagten, W.J.M. Dejonge, M. Demianiuk, Phys. Rev. B 36 (1987) 7013.

[65] H.T. Diep, A. Ghazali, P. Lallemand, J. Phys. C. Solid State 18 (1985) 5881.

[66] M.A. Boselli, A. Ghazali, I.C.D. Lima, Phys. Rev. B 62 (2000) 8895.

[67] X. Gratens, E. ter Haar, V. Bindilatti, N. Oliveira, Y. Shapira, M. Liu, Z. Golacki, S. Charar, A. Errebbahi, J. Phys.: Condens. Matter 12 (2000) 3711.